Bull Volcanol (1998) 59:281–290

ORIGINAL PAPER

Youxue Zhang

Experimental simulations of gas-driven eruptions: kinetics of bubble growth and effect of geometry

Received: 16 May 1997 / Accepted: 11 October 1997

Abstract Simulated gas-driven eruptions using CO_2–water-polymer systems are reported. Eruptions are initiated by rapidly decompressing CO_2–saturated water containing up to 1.0 wt.% CO_2. Both cylindrical test cells and a flask test cell were used to examine the effect of magma chamber/conduit geometry on eruption dynamics. Bubble-growth kinetics are examined quantitatively in experiments using cylindrical test cells. Uninhibited bubble growth can be roughly expressed as $dr/dt \approx \lambda D(\beta\text{-}1)/(\gamma t^{1/3})$ for a CO_2–water-polymer system at 0–22 °C and with viscosities up to 5 Pa·s, where r is the radius of bubbles, λ and D are the Ostwald solubility coefficient and diffusivity of the gas in the liquid, β is the degree of saturation (decompression ratio), and γ characterizes how the boundary layer thickness increases with time and is roughly 1.0×10^{-5} m/s$^{1/3}$ in this system. Unlike the radius of cylindrical test cells, which does not affect the eruption threshold and dynamics, the shape of the test cells (flask vs cylindrical) affects the dynamics but not the threshold of eruptions. For cylindrical test cells, the front motion is characterized by constant acceleration with both Δh (the height increase) and ΔV (the volume increase) being proportional to t^2; for the flask test cell, however, neither Δh nor ΔV is proportional to t^2 as the conduit radius varies. Test-cell geometry also affects foam stability. In the flask test cell, as it moves from the wider base chamber into the narrower conduit, the bubbly flow becomes fragmented, affecting the eruption dynamics. The fragmentation may be caused by a sudden increase in acceleration induced by conduit-shape change, or by the presence of obstacles to the bubbly flow. This result may help explain the range in vesicularities of pumice and reticulite.

Editorial responsibility: J. Fink

Youxue Zhang
Department of Geological Sciences, University of Michigan, Ann Arbor, MI 48109–1063, USA
Fax: +1(734) 763 4690
e-mail: youxue@umich.edu

Key words Gas-driven eruptions · Explosive volcanism · Limnic eruptions · Pumice · Experimental volcanology · Bubble growth · Vesicularity

Introduction

Gas-driven eruptions are powered by the exsolution of gas initially dissolved in a liquid. Two types of gas-driven eruptions are known. The more familiar type is explosive volcanic eruptions driven by the exsolution of H_2O from a magma, examples of which include the 1991 eruption of Mount Pinatubo, the 1980 eruption of Mount St. Helens, the 1902 eruption of Mount Pelee, and the 79 A.D. eruption of Vesuvius. The other type is the recently recognized limnic eruptions driven by the exsolution of CO_2 from water, such as the eruptions of Lake Nyos in 1986 and Lake Monoun in 1984 (Kling et al. 1987; Sigurdsson et al. 1987; Sigvaldson 1989; Freeth et al. 1990; Zhang 1996). CO_2–driven water eruptions may also be common on Europa, a Galilean satellite of Jupiter (Crawford and Stevenson 1988).

Several experimental approaches have been developed recently to experimentally simulate gas-driven eruptions. Zhang et al. (1992, 1997) simulated gas-driven eruptions by rapidly decompressing CO_2–saturated water, resulting in explosive flows with constant acceleration. Besides examining the dynamics of gas-driven eruptions, the effect of viscosity on eruption dynamics was investigated by adding an organic polymer to the solution (Zhang et al. 1997). Mader et al. (1996) investigated gas-driven eruptions by injecting K_2CO_3 solution into HCl solution. The mixing of the two solutions leads to the reaction between H^+ and CO_3^{2-} to form H_2CO_3, which decomposes to CO_2 (and H_2O) and results in explosive flows with very high but nonconstant accelerations. Mader et al. (1994) reported preliminary results from both Mader et al. (1996) and Zhang et al. (1997). Phillips et al. (1995) used a gum rosin and acetone system as an analog to examine the effect of vola-

tile-concentration-dependent viscosity. All of the above experimental studies examine a large range of processes of gas-driven eruptions, including bubble nucleation and growth, development of bubbly flow, foam formation and fragmentation, and eruption dynamics. Alidibirov and Dingwell (1996) carried out experiments to study the fragmentation of Mount St. Helens gray dacite. Lorenz et al. (1994) and Zinmanowski et al. (1997) examined the interaction and mixing of water and magma. The different experimental techniques complement each other, but quantitative comparisons between the results are not straightforward owing to a lack of scaling laws and to differences in techniques.

Previous simulations provide much information on the dynamics and kinetics of gas-driven eruptions and also point to new directions for further study:

1. Earlier experiments used cylindrical test cells with smooth walls as an analog of both the magma chamber and the eruption conduit. It is of interest to examine the effect of magma chamber and conduit geometry on eruption dynamics. An abrupt change in the conduit diameter is expected to cause a change in eruption velocity, which may induce fragmentation of the bubbly flow and alter the dynamics.
2. Bubble growth plays a critical role in eruption dynamics. Zhang et al. (1997) studied the time dependence of bubble radius in several experiments and showed that $r \approx at^{2/3}$ in a given experiment. A detailed study of bubble-growth kinetics using high-resolution close-up films is necessary to examine the quantitative relations between bubble-growth coefficient a and experimental conditions such as decompression ratio, viscosity, and temperature. Such quantitative relations would allow modeling of bubble growth in eruptions.
3. Earlier experiments showed that a viscosity increase from 0.001 Pa·s (for pure CO_2–water system) to 0.02–0.7 Pa·s (for CO_2–water-polymer systems) results in major changes in eruption dynamics especially in foam stability (Zhang et al. 1997). The 0.5–19 Pa·s experiments by Phillips et al. (1995) using a gum rosin and acetone system showed yet different dynamics where bubbles nucleate and grow only at the interface, instead of everywhere in the solution. Since viscosity of hydrous silicic magma is typically 10^6 Pa·s, it is important to carry out experiments at higher viscosities in the CO_2–water-polymer system to examine whether there would be other major changes in eruption dynamics.

New experiments examining bubble-growth kinetics with close-up motion picture photography are reported in this paper, as well as the effects of conduit geometry, liquid viscosity, and liquid temperature on eruption dynamics. The experiments simulate a range of processes in gas-driven eruptions, from bubble nucleation and growth to eruption. Because of the complexity of natural gas-driven eruptions and differences in scale between natural and simulated eruptions, direct quantitative application of the experimental results to natural eruptions is not straightforward and is not the purpose of this work. Rather, one type of gas-driven eruption (CO_2–driven water eruption) is simulated in order to gain an understanding of the basic physics of the eruptive process. The new experimental results reveal quantitatively the dependence of bubble-growth kinetics on experimental conditions and show how geometry of the conduit plays an important role in controlling eruption dynamics.

Experimental methods and conditions

The experiments were conducted in the Graduate Aeronautical Laboratories of California Institute of Technology. The experimental apparatus and procedures are similar to those of Zhang et al. (1997) and are summarized below. The apparatus consists mainly of a test cell and a large tank (Fig. 1). Ten experiments were carried out using cylindrical test cells (25.4 mm ID and either 0.254 m long or 0.456 m long) to examine bubble-growth kinetics, and the effects of viscosity and temperature. Fifteen experiments were carried out using a newly fabricated flask test cell (consisting of a cylindrical base 66 mm in diameter and a cylindrical neck 25 mm in diameter; Fig. 1) to examine the effect of geometry on eruption dynamics. Before the experiment, the test cell and the tank (Fig. 1) were separated by an Al foil diaphragm. Air in the test cell was evacuated to ≤ 0.1 kPa. The test cell was then partially filled with CO_2–saturated water at a CO_2 pressure of 359–690 kPa with or without an organic polymer that increased the viscosity. For cylindrical test cells, the initial CO_2–water solution filled 0.088 to 0.25 m of the cell. For the flask test cell, the initial solution was always completely within and usually filled roughly half

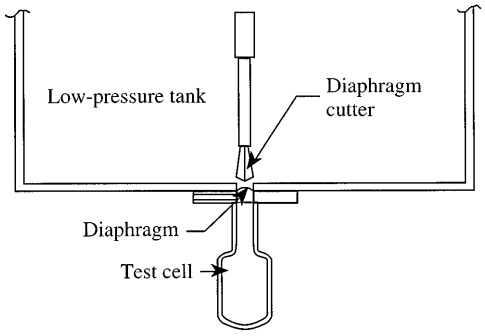

Fig. 1 A sketch of the experimental apparatus with the flask test cell. The experimental apparatus consists mainly of a test cell and a large tank (diameter = 0.61 m and height = 0.91 m) above the test cell. The flask test cell consists of a wide cylindrical base 66 mm in diameter and 80 mm long (analog of the magma chamber) and a narrow cylindrical neck 25 mm in diameter and 70 mm long (analog of the eruption conduit) connected by a transitional zone ~20 mm long. See Zhang et al. (1997) for the experimental setup with cylindrical test cells. Two cylindrical test cells are used in this study (see Table 1)

of the base chamber. The remaining upper part of the test cell was initially occupied by CO_2 gas. The tank was evacuated to a low pressure (4.8–9.9 kPa). At the beginning of the experiment, a cross-shaped knife inside the tank came down and cut the Al diaphragm. The pressure in the test cell was thus reduced, leading to oversaturation and eruption of the CO_2–water solution.

Conditions of all experiments are reported in Table 1. After each experiment, the amount of liquid still remaining in the test cell was measured and used to determine the eruption threshold. The eruption process typically lasted less than 1 s for cylindrical test cells and longer for the flask test cell. Eight of 10 experiments using cylindrical test cells, and 7 of 15 experiments using the flask test cell, were recorded by high-speed motion picture photography at 4000–6000 frames per second (fps). (Videos of the experiments are available from the author.) The high-speed films are used to study the details of the eruption process. The other experiments were used to examine the conditions for eruption. The films for all experiments with cylindrical test cells were close-up shots to investigate bubble growth in detail, since Zhang et al. (1997) took many films of experiments with cylindrical test cells to examine the other aspects of eruptions. With the exception of one (Run 174), these films centered roughly at the initial liquid–gas interface. The films for the seven experiments using the flask test cell examined the processes in the entire test cell (no close-up shots). Except for one (153), the films recorded experiments with eruptions. The films were examined for the motion of the eruption front by measuring the position of the front in successive film frames. Other phenomena, including foam formation and fragmentation, were also investigated.

In order to examine the effect of viscosity on eruption dynamics, 4 of the 15 filmed experiments (three for a cylindrical test cell, and one for the flask test cell) used a solution with a viscosity of ~ 5 Pa·s (5000 times the viscosity of water) by adding 1.0 wt.% of a polymer (Natrosol hydroxyethylcellulose HHR, Aqualon) to water. The experiments were time-consuming because the flow of the solution into the test cell was slow and because it took many hours for bubbles to ascend and escape from the solution.

Most experiments were carried out at room temperature but two experiments (176 and 177 in Table 1) were conducted at lower temperatures to examine the temperature effect. After the test cell was filled with CO_2–saturated water, an ice-water bath was used to cool the solution in the test cell. Just before the initiation of each experiment, the ice-water bath was removed to allow motion picture photography of the ex-

Table 1 Experimental conditions

Run no.	T (°C)	P_{tank} (kPa)	P_{cell} (kPa)	TC type	h_0 (m)	Polymer added (type, %)	η (Pa·s)	Film speed (fps)
Cylindrical test cells								
167	19.1	6.9	541	L1	0.124	None	0.001	No film
168	19.0	6.9	545	L1	0.120	None	0.001	4000
169	19.1	10.3	680	L1	0.124	None	0.001	4000
170	19.1	99	549	L1	0.243	None	0.001	No film
171	19.1	6.9	547	L1	0.247	None	0.001	4000
172	19.5	3.4	534	L1	0.176	HHR, 1%	5	4000
173	19.0	9.7	389	L1	0.181	HHR, 1%	5	6000
174	18.0	6.9	547	L1	0.088	HHR, 1%	5	6000
176	0–4	6.9	569	S	0.110	None	0.001	4000
177	0–4	8.3	519	S	0.100	None	0.001	4000
Flask test cell								
153	19.4	6.9	380	F	0.024	None	0.001	4000
154	19.7	6.9	552	F	0.045	None	0.001	No film
155	20.0	6.9	414	F	0.050	None	0.001	No film
156	19.9	6.9	621	F	0.058	None	0.001	No film
157	19.7	6.9	586	F	0.062	None	0.001	4000
158	20.0	6.9	347	F	0.062	None	0.001	No film
159	19.7	6.9	451	F	0.058	None	0.001	No film
160	18.4	6.9	555	F	0.064	None	0.001	4000
161	19.0	3.4	279	F	0.065	None	0.001	No film
162	20.0	10.5	685	F	0.064	None	0.001	No film
163	19.6	6.9	352	F	0.063	None	0.001	No film
164	19.4	6.9	690	F	0.066	None	0.001	4000
165	19.3	9.9	689	F	0.050	None	0.001	4000
166	19.3	4.8	359	F	0.061	None	0.001	4000
175	17.0	6.9	578	F	0.041	HHR, 1%	5	6000

TC (test cell) type: F = flask test cell (Fig. 1); L1 = cylindrical test cell with 0.0254 m ID and 0.456 m long; S = cylindrical test cell with 0.0254 m ID and 0.254 m long. h_0 is the initial front height (liquid column height). η is viscosity. Film speed is in frames per second (fps)

periment. The temperature of the solution in the test cell was measured to be ~4 °C after the experiment and after the test cell was vented and dismounted from the apparatus; hence, the temperature of the solution during the experiment was 0–4 °C.

Experimental results

General

Some quantitative experimental results are summarized in Table 2. For experiments with eruptions, a short time (defined as the incubation time, typically ≤13 ms) after the diaphragm is ruptured, CO_2 bubbles nucleate roughly in a single event (lasting for ~1 ms), implying heterogeneous nucleation (Zhang et al. 1997). These bubbles grow roughly at the same rate, leading to volume expansion and the upward motion of the expanding solution. The bubbles are initially roughly spherical, and then become oblate with the short axis oriented vertically, and then may become tear-drop shaped. Besides the overall upward expansion, bubbles also slowly rise buoyantly relative to the liquid. The conditions for eruption, upward motion of the eruption front, and bubble growth are examined in detail below.

Eruption threshold

The percentage of liquid loss in each experiment is reported in Table 2. An eruption is defined as an event with significant liquid ejection (≥5%) from the test cell. Zhang et al. (1997) showed that whether there is an eruption depends on the decompression ratio β (=initial test cell pressure divided by tank pressure; β may also be referred to as the degree of saturation, and β-1 the degree of supersaturation) and that there is a threshold decompression ratio of roughly 50 for cylindrical test cells and for pure CO_2–water system, i.e., there is rarely an eruption when $\beta<50$ and almost always an eruption when $\beta>50$. New experiments using cylindrical test cells are consistent with this conclusion (Fig. 2). The pressure differential (initial test-cell pressure minus the tank pressure) does not determine whether there is an eruption. If the percentage of liquid loss is plotted against the pressure differential, there is

Table 2. Experimental results

Run no.	β	Liquid loss (%)	a_f (m/s^2)	t_0 (ms)	a_f/h_0 (s^{-2})	α (m/s$^{2/3}$)
Cylindrical test cells						
167	78	59		No film		
168[a]	79	48	123 ± 12	38	1025	0.024
169[a]	66	41	57 ± 2	3.7	460	0.019
170	5.6	0		No film		
171[a]	79	76	122 ± 7	3.9	494	0.024
172[a]	155	100	176 ± 8	7.8	1000	0.038
173[a]	40	100	1.88 ± 0.03	6.9	10	0.007
174[a]	79	100		The front is not initially in the view		
176[a]	82	40	5.8 ± 0.5	11	53	0.016
177[a]	63	44	7.3 ± 0.2	2.0	73	0.011
Flask test cell						
153	55	0		No eruption		
154	80	20		No film		
155	60	10		No film		
156	90	28		No film		
157	85	29	23 ± 2	9.6	371	
158	50	3		No film		
159	65	16		No film		
160	80	33	29 ± 8	12.7	453	
161	81	45		No film		
162	65	38		No film		
163	51	35		No film		
164	100	48	67 ± 6	8.4	1015	
165	69	26	31 ± 1	12.7	620	
166	74	24	13 ± 1	6.6	213	
175	84	100	37 ± 1	10.1	298	

NOTE: $\beta=P_{cell}/P_{tank}$
Liquid loss is determined by measuring the amount of the solution still remaining in the test cell after the experiment (not based on film) and hence may be slightly different from films because of the dripping of liquid back to the test cell
a_f (acceleration of the front) and t_0 (incubation time) are obtained by fitting $\Delta h=0.5a_f(t-t_0)^2$ (Zhang et al. 1997), where Δh is the front height above the original liquid surface. For experiments using the flask test cell, only the part of the motion inside the cylindrical base chamber is used to obtain a_f and t_0. Errors are the fitting errors (with equal weight to each Δh value even tough some Δh values have greater uncertainties) given at the 2-σ level
α ($=r/t^{2/3}$) values are obtained by fitting bubble-growth data from close-up shots using $r=\alpha t^{2/3}$. The fits are for typical bubbles (not the rare large and small bubbles) in an experiment. The relative uncertainty of α is ~20%
[a] Close-up shots

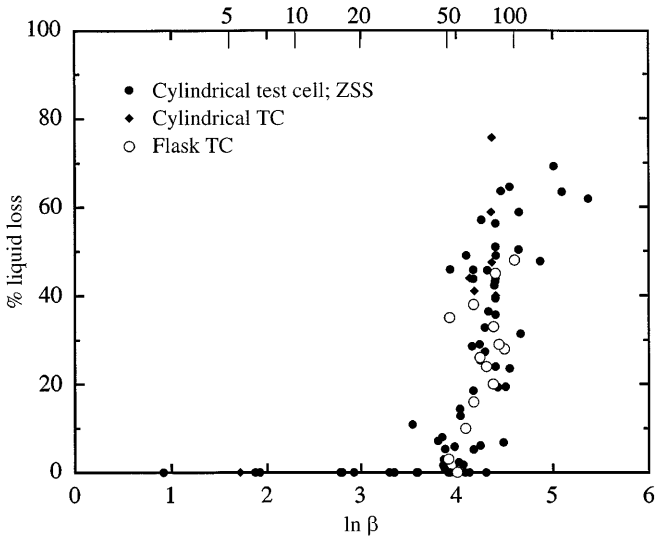

Fig. 2 Comparison of experimental results using cylindrical test cells [*filled circles;* from Zhang et al. 1997 (*ZSS*); *filled diamonds;* this work] and those using a flask test cell (*open circles;* this work). The percentage of liquid ejected from the test cell in an experiment is plotted against $\ln\beta$, where β is the decompression ratio. Only the data for the pure CO_2–water system (not those for higher-viscosity liquids) are shown for clarity. Owing to the dripping of water and other factors, there is some scatter in the liquid-loss data. Nevertheless, there is clearly a critical decompression ratio ($\sim$50), referred to as the eruption threshold, below which there is no liquid loss and above which there is significant liquid loss. The threshold is independent of the geometry of the test cell

no critical pressure differential above which there is an eruption and below which there is no eruption. For example, there is no eruption in Run 170 with a large pressure differential of 450 kPa (but a small β of 5.5), but there is an eruption in Run 161 with a small pressure differential of 276 kPa (but a large β of 82).

At a constant decompression ratio, the fraction of liquid ejected from the test cell increases for high viscosity liquids (Table 2), in agreement with the results of Zhang et al. (1997). This result is consistent with the understanding that increasing viscosity leads to more violent eruptions due to the retention of bubbles in liquids (instead of escaping by rising to the surface of the liquid), although the most important factor in violent eruption may be the number density of bubbles (Verhoogen 1951).

Whether the eruption threshold depends on the test-cell geometry is examined by comparing results from experiments using the flask test cell with those using cylindrical test cells (Fig. 2). The eruption threshold for experiments using the flask test cell is also at $\beta_c \approx 50$ for pure CO_2–water solution, the same as that using cylindrical test cells. Therefore, the shape of the test cell apparently does not affect the eruption threshold.

Experiments with cylindrical test cells

Besides the eruption threshold, experiments using cylindrical test cells are used to examine the rise of the flow front, bubble nucleation and growth, and the effect of viscosity and temperature on eruption dynamics. The flow front is defined as the interface between bubbly material and the gas phase. If bubbles at the front break up and the gas escapes, that gas is no longer treated as part of the bubbly material. This definition is for practicality since it is impossible to trace the gas escaped from bubbles. The front motion is characterized by constant acceleration (Zhang et al. 1997). The acceleration for each experiment is listed in Table 2.

Individual bubbles can be clearly seen in the close-up shots (except for Run 174) allowing bubble growth data to be obtained. Since the bubbles that are studied are at the top layer of the solution, it is assumed that bubble sizes observed in the top layer are the same as those in the bulk liquid. Zhang et al. (1997) showed that bubble growth during a CO_2–driven water eruption is not purely diffusion controlled and not proportional to $t^{1/2}$. Rather, owing to convection, bubble radius (r) grows as

$$r \approx \mathrm{a}t^{2/3}, \tag{1}$$

where t is the time since the appearance of the bubbles and α is a constant for each bubble. Since most bubbles in an experiment grow at a similar rate, α for each experiment is roughly constant. The α values obtained by fitting bubble growth data to Eq. (1) are shown in Table 2. The dependence of α on experimental conditions is discussed later.

The experiments at 0–4 °C show slower acceleration at the same decompression ratio than those at room temperature, as might be expected since both bubble nucleation density and the diffusivity of the gas component are expected to decrease with decreasing temperature. The effect of temperature on bubble growth rates is quantified later.

High-viscosity experiments

In all four 5-Pa·s experiments (including both cylindrical and flask test cells), the foam is more stable than that in 0.001-Pa·s pure CO_2–water liquid. The fraction of liquid loss at a given decompression ratio is higher than that in 0.001-Pa·s liquid. Bubbles are observed to nucleate roughly uniformly in the solution. All these results are consistent with those of Zhang et al. (1997) for polymer-bearing solutions (0.02–0.7 Pa·s). However, Phillips et al. (1995) observed bubble nucleation and growth only at the front in experiments using gum rosin and acetone at 0.5–19 Pa·s. The difference in bubble nucleation and growth styles between CO_2–water-polymer systems at 0.001 to 5 Pa·s (Zhang et al. 1992, 1997; Mader et al. 1994) and gum rosin-acetone systems at 0.5–19 Pa·s (Phillips et al. 1995) is not caused by viscosity differences, since there is a large viscosity overlap between the two sets of experiments. At present, the cause for the difference is not clear.

Experiments with the flask test cell, before the flow enters the narrower conduit

Dynamics of eruptions using the flask test cell before the flow enters the narrower part are similar to those using cylindrical test cells, as expected. Figure 3 shows the ascent of the front as a function of time for several experiments by plotting Δh (the distance traveled by the front) against $(t–t_0)^2=(\Delta t)^2$. Before the front encounters the narrower transition zone and neck, the ascent of the erupting front is characterized by a constant acceleration, similar to the results for cylindrical test cells. By fitting such data, the incubation time and the acceleration of the front before the flow enters the narrower part can be obtained (Table 2).

The incubation time is the time for the gas and solution in a test cell to decompress plus the time required for CO_2 bubbles to nucleate in the CO_2–oversaturated solution. There is much scatter in the incubation time, probably reflecting the random nature of nucleation and small differences in the purity of the water and the CO_2 gas (e.g., the presence of tiny dust particles) used in the experiments. The incubation time for nucleation seems slightly longer for experiments using the flask test cell (6–13 ms) than those using cylindrical test cells (2–11 ms except for Run 168 with 38 ms). If this difference is real, it may reflect the longer time required to decompress the gas phase above the liquid in a flask test cell because the gas in the wider chamber must escape through the narrow neck to the tank.

The front accelerations for experiments using the flask test cell before the flow enters the narrower part (Table 2) are typically smaller than those for cylindrical test cells. However, when normalized to the initial solution height (a_f/h_0 in Table 2), the front accelerations are similar in both sets of experiments. The dependence of front acceleration on the initial solution height under otherwise identical conditions is expected, because for the cylindrical part of a test cell, $\Delta h=h_0N(4\mathrm{p}r^3/3)$ where h_0 is the initial front height, N is number density of bubbles, and r^3 is the average cube of bubble radius (Zhang et al. 1997). Therefore, the front acceleration $a_f=\mathrm{d}^2(\Delta h)/\mathrm{d}t^2=h_0\mathrm{d}^2[N(4\pi r^3/3)]/\mathrm{d}t^2$ is expected to be proportional to h_0 when the flow is still in the cylindrical base.

In summary, before the flow enters the narrower part of the test cell, the eruption dynamics for experiments using the flask test cell are similar to those using the cylindrical test cell. Combining this result with the similarities of the eruption threshold, it can be inferred that test-cell radius (25 mm for the cylindrical test cells vs 66 mm for the base chamber part of the flask test cell) does not significantly affect the eruption threshold and dynamics in terms of acceleration and velocity (of course, the radius of the erupting conduit affects the volume eruption rate). Thus, the wall effect on the gas–liquid flow is not significant. By inference, the difference in the ratio of conduit diameter to bubble di-

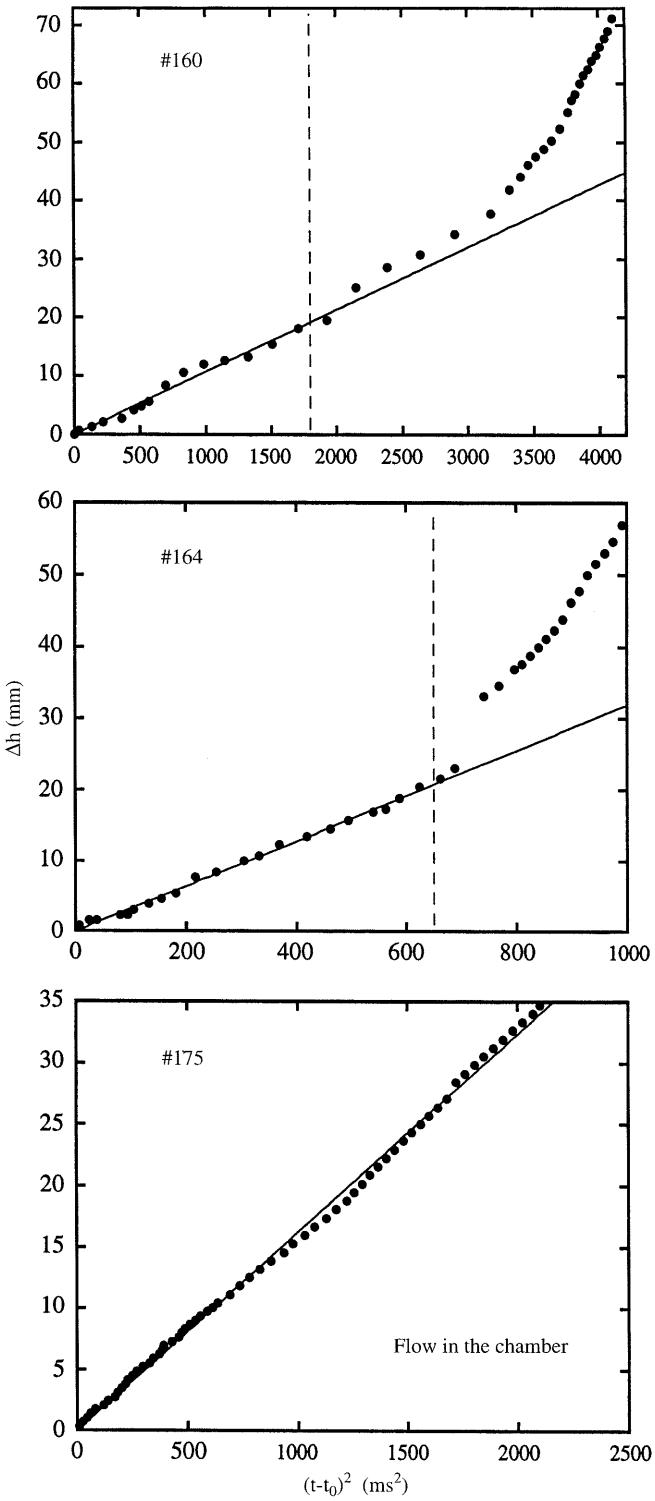

Fig. 3 Δh vs $(t–t_0)^2$ where Δh is the front height above the original liquid surface and t_0 is the incubation time (Zhang et al. 1997). The *dashed vertical lines* show roughly the time when the flow begins to enter the narrower neck. The *solid lines* are fits to data before the flow enters the narrower neck. For experiment 175, the front height after the flow enters the narrower neck cannot be obtained because the front is not clearly defined

ameter between natural and simulated eruptions causes no scaling problem.

Experiments with the flask test cell, after the flow enters the narrower conduit

Once the bubbly flow enters the narrower part of the flask test cell, the flow dynamics become different from those in a cylindrical test cell. The main results and differences are summarized below:

1. Figure 3 shows the motion of the front as a function of $(\Delta t)^2$. After the flow front moves from the base chamber into the narrower neck (on the right-hand side of the vertical dashed line in Fig. 3), Δh is no longer proportional to $(\Delta t)^2$. Thus, the acceleration is not constant but increases rapidly with time. This increase is expected, because the mass flow must pass through a narrower conduit. The flow velocity in the narrower neck is typically several meters per second. For example, for Run 164, the flow velocity in the neck is roughly 6 m/s, compared with 0–2 m/s in the lower and wider cylindrical base.
2. The above result, that Δh is not proportional to $(\Delta t)^2$ for a flask test cell, is not surprising since the radius varies, but one may expect that ΔV $(=V_{\text{bubbly liquid}}-V_0$, where ΔV is volume increase of the bubbly liquid and V_0 is the initial volume of the gas-saturated liquid) is proportional to $(\Delta t)^2$ for flask experiments even after the flow enters the narrower neck. This expectation arises because the proportionality between Δh and $(\Delta t)^2$ in cylindrical test cells is ultimately caused by the proportionality between ΔV and $(\Delta t)^2$ (Zhang et al. 1997). The variation in the radius of the test cell is expected to affect the relation between Δh and $(\Delta t)^2$, but not necessarily the relation between ΔV and $(\Delta t)^2$. To test the above consideration, V as a function of h for the flask test cell has been obtained by measuring the mass of distilled water in the test cell as a function of h. This V–h relation is not perfect, because the determination of h is not very accurate owing to the curved bottom of the test cell. Using the V–h relation, ΔV is estimated from Δh and plotted against $(\Delta t)^2$ for two experiments in Fig. 4. Though scattered, the data show that after the flow enters the narrower neck, ΔV is not proportional to $(\Delta t)^2$, contrary to what one might expect. ΔV increases with $(\Delta t)^2$ but at a rate slower than that in experiments with cylindrical test cells.
3. Observing the flow from the film at any fixed position in the narrow neck (or at the exit by inference), the flow is at a quasi-steady state after the flow enters the narrow neck, i.e., for a relatively long time (ca. 1 s), the flow characteristics (including velocity, fragmented nature, etc.) at a fixed position change only slowly as a function of time. This result is expected, because the amount of CO_2–oversaturated solution in the base chamber is large and mass flow through the narrow neck is slow.
4. The entering of the flow from the base chamber to the narrower neck is observed to be accompanied by fragmentation, even at a vesicularity less than 74% and even for a viscous fluid (5 Pa·s for Run 175). Thus, the foam in the base chamber, but not in the neck, is stable to a high vesicularity. This result contrasts with the case of cylindrical test cells in which fragmentation occurs roughly at 70–80% vesicularity for low viscosity liquids but does not occur at 97% vesicularity for liquids with viscosities of 0.02–0.7 Pa·s (Zhang et al. 1997). The fragmentation as the flow enters the narrower conduit might be the cause for nonproportionality between ΔV and $(\Delta t)^2$.

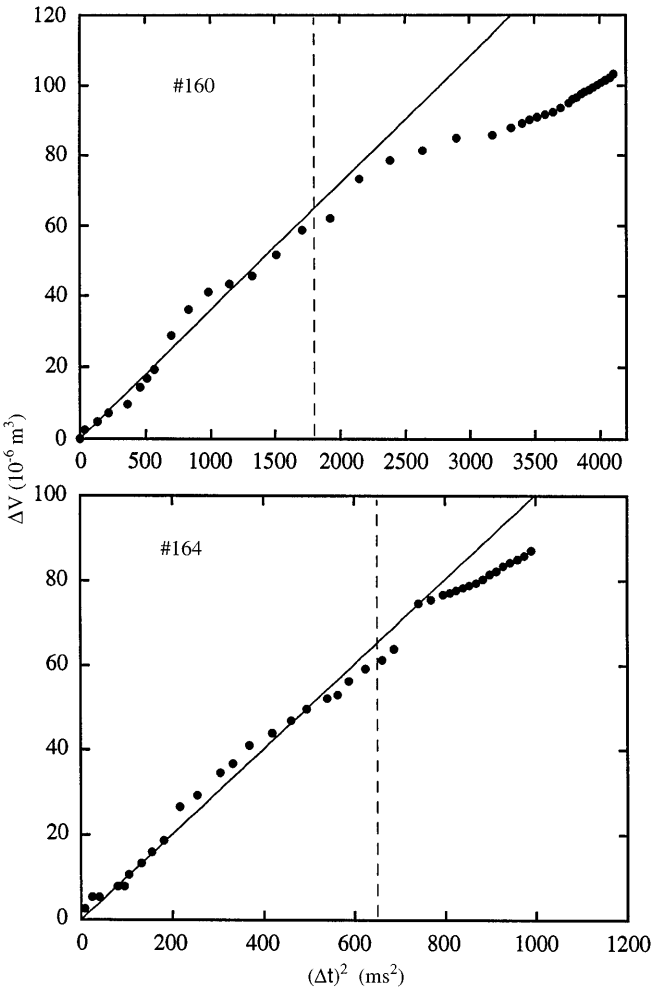

Fig. 4 ΔV vs $(\Delta t)^2$ where ΔV is the volume increase of the bubbly liquid and $\Delta t = t - t_0$. The *dashed vertical lines* show the time when the flow enters the narrower neck. The *solid lines* are fits to data before the flow enters the narrower neck

The above differences show that the geometry of the test cell significantly affects eruption dynamics once the flow enters the part of the test cell with variable radius. Some of these differences are expected, whereas others are not.

Discussion

Bubble growth

The new bubble-growth data from the close-up shots are used to examine how bubble growth depends on experimental conditions. The relation between the bubble-growth parameter α in Eq. (1) and the experimental conditions can be approximately modeled as follows. Bubble-growth rate can be expressed as (Zhang et al. 1997):

$$dr/dt \approx [(C_0 - C_s)/\rho]D/\delta \approx \lambda D(\beta\text{-}1)/\delta, \quad (2)$$

where D is the CO_2 diffusivity in the solution, δ is the boundary layer thickness that depends on time, C_0 is the bulk CO_2 concentration in the solution, C_s is the CO_2 concentration in the liquid bubble wall, and ρ is the concentration of CO_2 in the gas phase (all concentrations are in mol/m^3 or kg/m^3). Ignoring surface tension (for bubbles of ≥ 0.1 mm size), and assuming (a) CO_2 concentration in the liquid away from the boundary layer is the same as the initial concentration (i.e., bubble radius is measured before bubbles interact with one another), and (b) surface equilibrium (i.e., $C_s/\rho = \lambda$ where λ is the Ostwald solubility coefficient), then, $(C_0 - C_s)/\rho$ can be expressed as $\lambda(\beta\text{-}1)$ where β-1 is the degree of supersaturation, resulting in the second approximation in Eq. (2). To determine the dependence of δ in Eq. (2) on time, Eq. (1) is rewritten as

$$dr/dt = (2/3)\alpha t^{-1/3}. \quad (3)$$

For simplicity, the dependence of δ on r is ignored. Combining Eqs. (2) and (3) leads to

$$\delta \approx [1.5\lambda D(\beta\text{-}1)/\alpha]t^{1/3} \equiv \gamma t^{1/3}. \quad (4)$$

The above equation defines the γ parameter that characterizes how the boundary-layer thickness increases with time. Local convection affects the boundary-layer thickness and γ. The relation between γ and α and other parameters can thus be obtained:

$$\alpha \equiv 1.5\lambda D(\beta\text{-}1)/\gamma. \quad (5)$$

Equation (5) shows that α is proportional to $(\beta$-1) at a given temperature and polymer composition if γ is roughly constant under such conditions. As shown in Fig. 5, for a given polymer composition and temperature, α is indeed roughly proportional to $(\beta$-1), demonstrating that the above simple consideration captures the essence of bubble-growth kinetics in the experiments. At constant β, α at 0–4 °C is approximately 63% of that at 19.1 °C, which is expected from Eq. (5) since D at 0–4 °C is 62% of that at 19.1 °C (Tamimi et al. 1994). Even though λ, and hence dissolved CO_2 content at a given P, increases as the temperature decreases, which would offset the effect of diffusivity decrease, the experimental procedure is such that the effect caused by λ increase would not be noticeable. The experimental solution was not prepared at 0–4 °C; rather, the solution was cooled after CO_2 was dissolved into it. Hence, the CO_2 concentration in the solution did not change during cooling. Specifically, it did not increase to the level that would correspond to equilibrium at 0–4 °C and at the pressure. Therefore, the value of $[(C_0 - C_s)/\rho] \sim \lambda(\beta\text{-}1)$ in Eq. (5) is not significantly affected by cooling the solution, and α is roughly proportional to D, as observed.

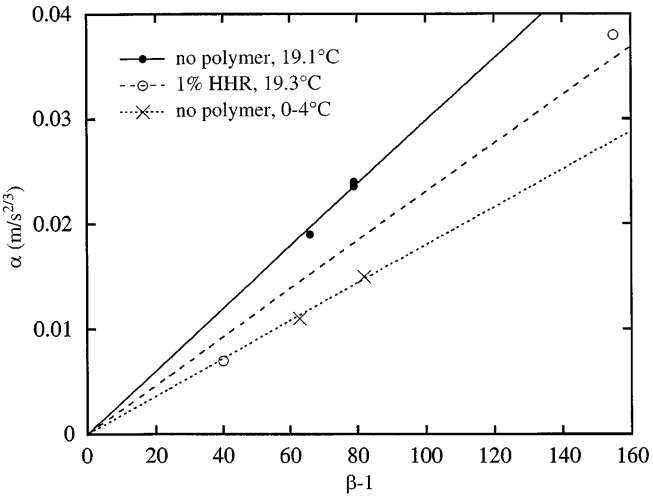

Fig. 5 Bubble-growth parameter α $(= r/t^{2/3})$ vs the degree of supersaturation $(\beta$-1) for three sets of experiments with cylindrical test cells. *Solid circles* are for pure CO_2–water system at 19.1 °C, *open circles* for CO_2–water system with 1% HHR added resulting in a viscosity of ~5 Pa·s, and *crosses* for pure CO_2–water system at 0–4 °C. The *lines* are simple least-squares fits to each group of data passing through the origin

It is also observed that at constant β, α in the 5-Pa·s solution is approximately 80% of that in 0.001-Pa·s solution. This decrease in bubble-growth rate may be caused by the small effect of adding polymers on increasing γ or decreasing D or λ. If all the effect is caused by a decrease in D_{CO2}, this small viscosity effect on D_{CO2} in CO_2–water-polymer solution (~20% decrease in D while η increases by a factor of 5000) follows neither the Einstein viscosity-diffusivity relation nor the Eyring relation in which diffusivity is inversely proportional to viscosity.

From experimentally determined α values, γ can be calculated from Eq. (5) using D from Tamimi et al. (1994) and λ from Dean (1985) but ignoring the variation of λ with temperature as discussed above. For six experiments without polymer addition (five in this work and Run 150 in Zhang et al. 1997) at both 19.1 and 0–4 °C, γ is independent of temperature and roughly constant, 0.9×10^{-5} m/s$^{1/3}$ (ranging from 0.8×10^{-5} to 1.1×10^{-5} m/s$^{1/3}$). For three experiments with polymer addition (two in this work and Run 89 in Zhang et al. 1997; Run 94 is not used because β is not known), if D_{CO2} is assumed to be unaffected by polymer addition, γ is roughly 1.2×10^{-5} m/s$^{1/3}$ (ranging from 1.0×10^{-5} to 1.4×10^{-5} m/s$^{1/3}$), 38% greater than γ in polymer-free solutions.

The slower bubble growth in experiments with polymer addition can be accounted for by either a small decrease of D_{CO2} due to a large increase of η or a small increase of boundary layer thickness (γ) due to a large increase of η. Both of these variations are expected and reasonable. On the other hand, the variation in bubble-growth rates is small and almost within the scatter of bubble growth rates in each experiment. Hence, it is not clear whether these variations are real. For simplicity, γ is treated as a constant in the CO_2–water-polymer system at 0–22 °C and viscosity of 0.001–5 Pa·s. The average value for γ in all experiments is 1.0×10^{-5} m/s$^{1/3}$. Thus, the boundary-layer thickness δ is roughly 1 mm at 1 ms and 10 mm at 1 s. The thickness is somewhat smaller than the diffusive boundary layer thickness ($\sqrt{Dt}$) of 1.4 mm at 1 ms and 40 mm at 1 s, demonstrating the role of local convection.

The constancy of γ (10^{-5} m/s$^{1/3}$) allows bubble radius to be estimated using

$$r \approx [1.5\lambda D(\beta\text{-}1)/\gamma]t^{2/3}, \quad (6)$$

to $\leq$40% relative uncertainty. The differential form of Eq. (6) is:

$$dr/dt \approx \lambda D(\beta\text{-}1)/(\gamma t^{1/3}), \quad (7)$$

which can be integrated to obtain bubble radius if the decompression ratio and/or other parameters vary with time.

Bubble growth in limnic eruptions

The apparent universality of Eq. (7) for CO_2–water solutions and the constancy of γ allow bubble growth in limnic eruptions (and in other situations where convection affects the boundary layer thickness) to be modeled by integration of the equation:

$$r = \int \lambda D(\beta\text{-}1)/(\gamma t^{1/3})dt, \quad (8)$$

if the dependence of β on time is known as the ambient pressure decreases with the ascent of the flow. The presence of impurities in lake water, though expected to increase the nucleation density and hence to decrease the eruption threshold by a large factor, is not expected to significantly affect bubble-growth kinetics. Using the maximum ascent velocity of limnic eruptions (Zhang 1996), assuming that CO_2 concentrations far away from bubbles are not affected by bubble growth (hence no rough equilibrium between bubbles and liquid), and carrying out the above integration numerically, the bubble diameter is 0.8 mm as the porosity of the bubbly flow reaches 74%. (Above this porosity, the bubbly flow is expected to fragment to a gas flow carrying water droplets; Zhang et al. 1997). Since the actual ascent velocity can be significantly smaller than the maximum ascent velocity (Zhang 1996), the bubble sizes as the porosity reaches 74% are probably significantly larger. Because the nucleation density in lake water is unknown, it is difficult to assess whether the above growth rate is high enough so that rough equilibrium between the gas and liquid phases can be maintained during a limnic eruption. A bubble nucleation density that is significantly greater than 10^{10} m^{-3} would be necessary to maintain rough gas–liquid equilibrium through bubble growth.

Nucleation

Nucleation is a one-time event in this study and previous experiments (Zhang et al. 1997) in which the ambient (tank) pressure is constant. Thus, the nucleation mechanism is almost certainly heterogeneous. Because the number of bubbles does not change significantly with time and all bubbles are roughly the same size, the front motion can be expressed as $\Delta h = 0.5 a_f t^2 = (4/3)\pi r^3 N h_0$. It follows that

$$a_f = (8/3)\pi\alpha^3 N h_0 = (8/3)\pi[1.5\lambda D(\beta\text{-}1)/\gamma]^3 N h_0 = 9\pi N h_0 [\lambda D(\beta\text{-}1)/\gamma]^3, \quad (9)$$

for cylindrical test cells. Using the above equation, number density (N) of bubbles can be estimated from a_f/h_0 and β. N thus estimated ranges from 10^6 to 10^9 for all experiments in this study and Zhang et al. (1997), in agreement with the results of Zhang et al. (1997). However, a consistent relation between N and β is not observed (nor between N and the pressure differential), probably reflecting small differences in the purity of the water or the CO_2 gas used in experiments, i.e., with a larger data set, the rough correlation between N and β observed in Zhang et al. (1997) with only two data points is not confirmed. Because the above section shows that α can be predicted well using Eq. (5), the uncertainty in number density of bubbles remains the only difficulty in predicting a_f in a cylindrical test cell, i.e., it is not possible to predict the dynamics of a simulated eruption even for a cylindrical conduit. According to Eq. (7), increasing (β-1) by a factor of 2 would increase bubble volume growth rate by a factor of 8. Hence, the front acceleration would increase at least by a factor of 8 for cylindrical test cells (ignoring the effect of increased decompression ratio on nucleation density). The strong dependence of bubble growth rate on (β-1) probably plays a main role in the dependence of the eruption threshold on the decompression ratio.

Foam fragmentation and vesicularity

Understanding the condition of fragmentation is very important for understanding the dynamics of gas-driven eruptions. Before fragmentation, the two-phase flow is bubbly, and its dynamics are largely controlled by the kinetics of bubble growth (mass transfer of the gas component from the liquid into the bubbles). After fragmentation, the two-phase flow is a gas flow carrying liquid droplets, and the dynamics are largely controlled by gas dynamics. Fragmentation of apparently benign

lava domes or flows may lead to deadly pyroclastic flows such as those at Mount Unzen in Japan (Fink and Kieffer 1993).

Zhang et al. (1997) showed that when the liquid viscosity is greater than 20 times that of water, a foam can be stable for vesicularities up to 97% in a smooth cylindrical test cell. This study shows that when the bubbly flow encounters the narrower part of the test cell, the foam may fragment. The fragmentation as the bubbly flow moves from the wider base chamber into the narrower neck is possibly caused by a sudden change in flow acceleration or by the obstruction of the narrowing wall to the bubbly flow. Pumice and reticulite with both high (up to 98%) and low vesicularities ($\sim$70%) have been found (Thomas et al. 1994; Cashman and Mangan 1994). The variable vesicularities in natural pumice and reticulite might be partially controlled by conduit smoothness. The higher-vesicularity pumice might reflect a relatively smooth conduit whose diameter varies only slowly with depth, whereas the lower-vesicularity pumice might reflect an uneven conduit (rough or rapid change in radius) or a low initial volatile content. Since an uneven conduit can be eroded away, the vesicularity of pumice may evolve with time in a single eruption.

Conclusion

Experiments in this study show that the geometry of the test cell (or conduit) plays an important role in controlling the eruption dynamics. Quasi-steady eruption is observed when a flask-shaped test cell is used, in contrast to transient eruption for cylindrical test cells. Besides the expected effect on acceleration and velocity, volume eruption rates and foam stability are also affected by the variable radius of the flask test cell. Fragmentation may be induced by a sudden change in conduit diameter. By inference, fragmentation may occur in an uneven conduit or be induced by a sudden change in flow velocity/acceleration. This type of fragmentation may affect vesicularity of pumices.

A detailed examination of the dependence of bubble-growth kinetics on experimental conditions using cylindrical test cells shows that bubble growth in CO_2–water-polymer systems can be quantified by $dr/dt \approx \lambda D(\beta\text{-}1)/(\gamma t^{1/3})$, where λ and D are the Ostwald solubility coefficient and diffusivity of the gas in the liquid, β is the degree of saturation, and γ characterizes how the boundary-layer thickness increases with time and is roughly 1.0×10^{-5} m/s$^{1/3}$. The quantification allows the prediction of convective bubble growth in CO_2–driven water eruptions. The number density of bubbles in experiments varies by several orders of magnitude, but the variation cannot be quantitatively related to experimental conditions at this time. Hence, bubble nucleation density remains an uncertainty in predicting the dynamics of gas-driven eruptions.

Acknowledgements I thank B. Sturtevant (Graduate Aeronautical Laboratory, California Institute of Technology) for providing the shock-tube apparatus for experiments reported here. Thanks also to Z. Xu, who helped obtain some of the data from films reported here. Comments by O. Navon, M. Alidibirov, E. J. Essene, J. Fink, J. Holloway, R. A. Lange, Z. Xu, and an anonymous reviewer greatly improved this paper. This work was partially supported by NSF grants EAR-93–04161 and EAR-94–58368.

References

Alidibirov M, Dingwell DB (1996) Magma fragmentation by rapid decomposition. Nature 380:146–148

Cashman KV, Mangan MT (1994) Physical aspects of magmatic degassing II. Constraints on vesiculation process from textural studies of eruptive products. Rev Mineral 30:447–478

Crawford GD, Stevenson DJ (1988) Gas-driven water volcanism and the resurfacing of Europa. Icarus 73:66–79

Dean JA (1985) Lange's handbook of chemistry. McGraw-Hill, New York, pp 1856

Fink JH, Kieffer SW (1993) Estimate of pyroclastic flow velocities resulting from explosive decompression of lava domes. Nature 363:612–615

Freeth SJ, Kling GW, Kusakabe M, Maley J, Tchoua FM, Tietze K (1990) Conclusions from Lake Nyos disaster. Nature 348:201

Kling GW, Clark MA, Compton HR, Devine JD, Evans WC, Humphrey AM, Koenigsberg EJ, Lockwood JP, Tuttle ML, Wagner GN (1987) The 1986 Lake Nyos gas disaster in Cameroon, West Africa. Science 236:169–175

Lorenz V, Zimanowski B, Frohlich G (1994) Experiments on explosive basic and ultrabasic, ultramafic, and carbonatitic volcanism. In: Meyer HOA, Leonardos OH (eds) Proc Fifth International Kimberlite Conference. Companhia de Pesquisa de Recursos Minerais, Rio de Janeiro, pp 270–282

Mader HM, Phillips JC, Sparks RSJ, Sturtevant B (1996) Dynamics of explosive degassing of magma: observations of fragmenting two-phase flows. J Geophys Res 101:5547–5560

Mader HM, Zhang Y, Phillips JC, Sparks RSJ, Sturtevant B, Stolper EM (1994) Experimental simulations of explosive degassing of magma. Nature 372:85–88

Phillips JC, Lane SJ, Lejeune AM, Hilton M (1995) Gum rosin-acetone system as an analogue to the degassing behavior of hydrated magmas. Bull Volcanol 57:263–268

Proussevitch AA, Sahagian DL (1996) Dynamics of coupled diffusive and decompressive bubble growth in magmatic systems. J Geophys Res 101:17447–17455

Sigurdsson H, Devine JD, Tchoua FM, Presser TS, Pringle MKW, Evans WC (1987) Origin of the lethal gas burst from Lake Monoun, Cameroon. J Volcanol Geotherm Res 31:1–16

Sigvaldason GE (1989) International Conference on Lake Nyos disaster, Yaounde, Cameroon, 16–20 March, 1987: conclusions and recommendations. J Volcanol Geotherm Res 39:97–107

Tamimi A, Rinker EB, Sandall OC (1994) Diffusion coefficients for hydrogen sulfide, carbon dioxide, and nitrous oxide in water over the temperature range of 293–368 K. J Chem Eng Data 39:330–332

Verhoogen J (1951) Mechanics of ash formation. Am. J. Sci. 249:729–739

Zhang Y (1996) Dynamics of CO_2–driven lake eruptions. Nature 379:57–59

Zhang Y, Sturtevant B, Stolper EM, Pyle D (1992) Gas-powered volcanic eruptions. I. Preliminary results of experimental simulations on initiation of eruption, front advance, and bubble growth. EOS 73:F628

Zhang Y, Sturtevant B, Stolper EM (1997) Dynamics of gas-driven eruptions: experimental simulations using CO_2–H_2O-polymer system. J Geophys Res 102:3077–3096

Zimanowski B, Buttner R, Lorenz V, Hafele H-G (1997) Fragmentation of basaltic melt in the course of explosive volcanism. J Geophys Res 102:803–814